Nanocrystalline Diamond Nanoelectrode Arrays and Ensembles

Jakob Hees,* René Hoffmann, Armin Kriele, Waldemar Smirnov, Harald Obloh, Karlheinz Glorer, Brian Raynor, Rachid Driad, Nianjun Yang, Oliver A. Williams, and Christoph E. Nebel

Fraunhofer Institute for Applied Solid State Physics, Tullastrasse 72, Freiburg 79108, Germany

ABSTRACT In this report, the fabrication of all-nanocrystalline diamond (NCD) nanoelectrode arrays (NEAs) by e-beam lithography as well as of all-diamond nanoelectrode ensembles (NEEs) using nanosphere lithography is presented. In this way, nanostructuring techniques are combined with the excellent properties of diamond that are desirable for electrochemical sensor devices. Arrays and ensembles of recessed disk electrodes with radii ranging from 150 to 250 nm and a spacing of 10 μm have been fabricated. Electrochemical impedance spectroscopy as well as cyclic voltammetry was conducted to characterize arrays and ensembles with respect to different diffusion regimes. One outstanding advantage of diamond as an electrode material is the stability of specific surface terminations influencing the electron transfer kinetics. On changing the termination from hydrogen- to oxygen-terminated diamond electrode surface, we observe a dependence of the electron transfer rate constant on the charge of the analyte molecule. $Ru(NH_3)_6^{+2/+3}$ shows faster electron transfer on oxygen than on hydrogen-terminated surfaces, while the anion $IrCl_6^{-2/-3}$ exhibits faster electron transfer on hydrogen-terminated surfaces correlating with the surface dipole layer. This effect cannot be observed on macroscopic planar diamond electrodes and emphasizes the sensitivity of the all-diamond NEAs and NEEs. Thus, the NEAs and NEEs in combination with the efficiency and suitability of the selective electrochemical surface termination offer a new versatile system for electrochemical sensing.

KEYWORDS: NCD · nanoelectrode array and ensemble · nanosphere lithography · impedance spectroscopy · diamond electrochemistry

There have been several reviews on the fabrication, characterization, and the analytical application of ultrasmall electrodes, with sizes down to a few nanometers.[1,2] Single nanoelectrodes offer various benefits compared to planar macroscopic electrodes such as low capacitive currents and decreased deleterious effects of solution resistance due to the small dimensions. Another advantage of nanoelectrodes arises from the radial diffusion to an electrode which is pointlike compared to the diffusion length. Due to the three-dimensional diffusion, there is an enhanced rate of mass transport to the electrode increasing the signal-to-noise ratio. However, single nanoelectrodes only generate small currents that are difficult to detect with conventional electrochemical setups. This can be circumvented by fabricating arrays or ensembles of electrodes that operate in parallel and amplify the measured currents.

Several techniques have been employed to fabricate nanoelectrodes and arrays or ensembles thereof from a wide range of material systems. The straightforward techniques to fabricate nanoelectrodes make use of e-beam lithography[3] and focused ion beam milling[4,5] structuring an insulating layer on top of a metal electrode. Less costly fabrication techniques apply nanoimprint techniques[3] and nanosphere lithography[6] to generate ordered nanoelectrode arrays. To achieve random ensembles of nanoelectrodes, different techniques are used such as the deposition of metals into pores of polycarbonate nanoporous membranes,[7−9] nanosphere lithography,[10] or block copolymer self-assembly.[11−13] Another approach utilizes spatially separated carbon nanofibers as a nanoelectrode sensor, showing promising properties for electrochemical sensing.[14−17]

Advantages of nanoelectrode arrays (NEA) and nanoelectrode ensembles (NEE) compared to planar electrodes are the low detection limit, an increased signal-to-noise ratio, and the possibility to conduct spatially and temporally resolved electrochemical measurements. For electrode arrays or ensembles, in general, to benefit from these characteristics, the dimensions of the array need to fulfill certain requirements. To reach a regime where hemispherical diffusion layers of neighboring electrodes do not overlap, the ratio of the interelectrode distance and the radius of a single electrode needs to be large enough depending on the time-scale of the experiment.[1,3,18,19] Therefore, an averaged interelectrode distance plays a crucial role in the fabrication of nanoelectrode ensembles.

Adding a supporting electrolyte is essential to conduct accurate electrochemical experiments on planar electrodes. This is to confine the ohmic drop between the

* Address correspondence to jakob.hees@iaf-extern.fraunhofer.de.

Received for review February 10, 2011 and accepted March 10, 2011.

Published online March 17, 2011
10.1021/nn2005409

working and counter electrode to a small region close to the electrode−liquid interface. Nano- and microelectrode arrays have been shown to offer the possibility to use either low concentrations of or even no supporting electrolyte, which also is desirable for various applications.[20,21]

The choice of electrode material determines the overall sensing properties of the device. Boron-doped diamond films offer several important properties that are essential for electrochemical sensing applications. Among others, these are wide potential windows, low background currents, fast electron transfer rates for various redox molecules, and adjustable stable surface terminations. Diamond films are chemically inert and show long-term response stability.[22] It is also reported that diamond offers several advantages in biosensing due to its extreme properties.[23−25]

Combining both the advantages of ultrasmall electrode arrays with the superior electrochemical properties of boron-doped diamond therefore results in a new class of electrochemical sensor devices. So far, the fabrication of diamond microelectrode arrays down to a size of 5 μm has been reported,[26−28] including the fabrication of all-diamond microelectrode arrays with electrode diameters from 10 to 25 μm.[27]

It is expected that the benefits arising from using microelectrode arrays are further emphasized by scaling down the electrode size into the submicrometer and nanometer range. To date, fabricated diamond microelectrode arrays applied microcrystalline boron-doped diamond as the electrode material. The drawback, however, in using microcrystalline diamond while downscaling the size of the electrode into the submicrometer regime is that boron-doping and thus electroactivity is inhomogeneous, depending on the orientation of grains of the diamond film.[29] For this reason, boron-doped microcrystalline diamond as a substrate for the fabrication of nanoelectrode arrays will result in nanoelectrodes with irreproducible inhomogeneous electrochemical activity when comparing neighboring electrodes depending on the grain orientation.

This issue is ruled out by using thin nanocrystalline diamond (NCD) films as a substrate since grain sizes vary from a few tens of nanometers up to 300 nm, resulting in electrodes containing several grains. Therefore, electrochemical activity is homogenized comparing single electrodes of the array. The usage of thin NCD films for the fabrication of NEE or NEA offers an additional advantage compared to single or microcrystalline diamond electrodes since NCD films are cheap and can be grown on large area substrates of up to several inches.

In this paper, we introduce the fabrication of all-nanocrystalline diamond NEAs and NEEs and their characterization by cyclic voltammetry and impedance spectroscopy. Furthermore, a surface termination effect on the electron transfer rate constant has been observed for redox analytes that has not been observed on macroscopic planar electrodes which will be discussed in detail in this paper.

RESULTS AND DISCUSSION

Fabricated nanoelectrode arrays and ensembles as described in the Methods section are shown in Figure 1. In Figure 1a,A, an overview of the NEA and the NEE is shown. Figure 1a indicates the hexagonally ordered array of electrodes, while Figure 1A demonstrates the random distribution of electrodes in the ensemble. Figure 1b,c illustrates different steps in the process to fabricate a nanoelectrode by e-beam lithography shown in Figure 1d. On the other hand, Figure 1B displays a SiO_2 sphere with insulating diamond grown around it and Figure 1C the exposed boron-doped nanoelectrode after removal of the sphere. Figure 1D sketches the cross section of the fabricated electrode arrays and ensembles, composed of a structured insulating NCD layer on top of a conductive boron-doped NCD film.

Initially, the nanoelectrode ensembles were characterized using conductive atomic force microscopy (C-AFM). First, the density of electrodes obtained from a SiO_2 sphere solution of the given concentration is derived from a large area scan of 50 μm $\times$ 50 μm. The density determined by AFM of 8.5×10^5 cm^{-2} is in good agreement with the expected values from the sphere concentration in the solution mentioned in the Methods section. The size of electrodes that are fabricated from spheres with a radius of 500 nm can be extracted from scans shown in Figure 2a−d to be 175 nm in radius. In Figure 2a, the topography of two neighboring electrodes is displayed with a corresponding scan of the current in Figure 2c. The cross sections below clarify the thickness of the insulating diamond layer in Figure 2b as well as the electrical properties of the boron-doped electrode and the insulating diamond in Figure 2d. It is clearly seen that the fabrication process yields conductive nanoelectrodes surrounded by 140 nm thick insulating diamond.

Electrochemical Characterization Using Cyclic Voltammetry. There have been several publications on the theoretical hemispherical diffusion to microdisk electrodes[18,19,30,31] as well as research on how voltammograms and impedance spectra change when varying the dimensions such as the size and the distance of electrodes of an array or an ensemble.[32] Three distinct diffusion regimes exist when investigating different time-scales of an experiment, such as the scan rate in cyclic voltammetry or the frequencies in impedance spectroscopy. These parameters determine the radii of the diffusion hemispheres around each single electrode in an array. In the case of very long time-scales of the experiment, diffusion layers overlap and the array acts as a macroscopic planar electrode showing peak

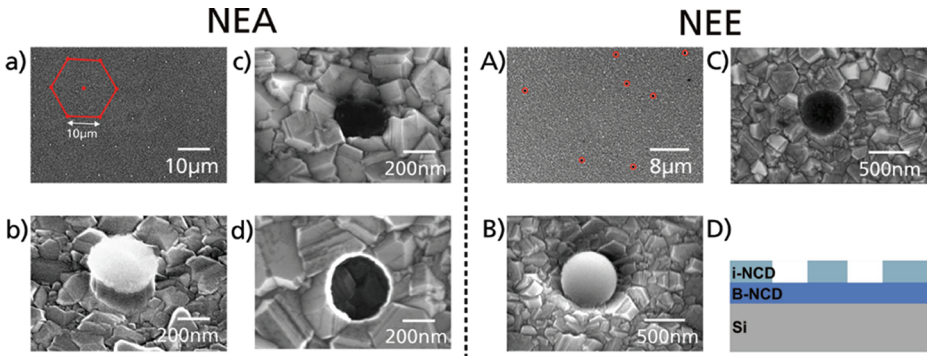

Figure 1. SEM images of a NEA and a NEE at different stages of the fabrication process: (a) overview of the design with distances of 10 μm of neighboring electrodes with hexagonal order (indicated in red), (b) structured SiO_2/Ni islands on boron-doped NCD layer, (c) insulating diamond grown around SiO_2, and (d) final recessed diamond electrode. (A) Overview of statistically distributed electrodes on boron-doped NCD substrate indicated by red circles, (B) SiO_2 sphere after growth of insulating diamond, (C) final boron-doped NCD electrode after removal of SiO_2, and (D) schematics of the cross section of fabricated electrodes.

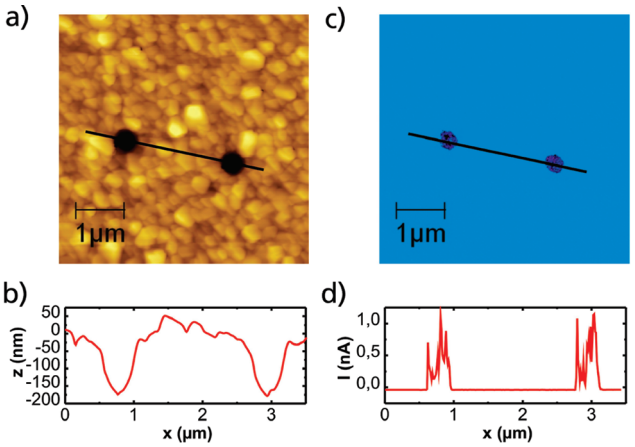

Figure 2. Conductive AFM scans of area 5 μm $\times$ 5 μm containing two electrodes: shown is (a) the topography, (b) the current at bias voltage 500 mV, and cross sections through two recessed electrodes for (c) the topography and (d) the current.

shaped voltammograms (Figure 3c). Increasing the scan rate or the frequency causes the diffusion layer thickness to decrease until diffusion hemispheres no longer overlap (Figure 3d). This diffusion regime yields sigmoidal voltammograms with steady-state hemispherical diffusion. The transition from overlapping to non-overlapping diffusion hemispheres is given by the characteristic frequency $\omega = D/d^2$,[32,33] where d is the distance of neighboring electrodes and D the diffusion coefficient of the analyte. By further increasing the frequency or scan rate, a regime is obtained where a single electrode can be considered a planar electrode and effects of the boundary of the single electrode become insignificant. The characteristic frequency that determines this regime is $\omega = D/a^2$ with the radius a of a single electrode.[19] In the interval given by these two frequencies, the electrode array shows a steady-state behavior of spatially separated nanoelectrodes.

Figure 3a,b displays cyclic voltammograms of 1 mM $Fe(CN)_6^{-3/-4}$ in 0.1 M KCl for various scan rates from a few millivolts/second up to 10 V/s on the NEA (Figure 3a) and the NEE (Figure 3b). For very small scan rates (20 mV/s for the NEA and 1 mV/s for the NEE), the voltammograms have mixed shapes, indicating partially overlapping diffusion hemispheres. Increasing the scan rate for both electrodes results in typical steady-state sigmoidal voltammograms with saturating steady-state currents for increasing scan rates. The graphs confirm that both the nanoelectrode array and the self-assembled nanoelectrode ensemble show the characteristics expected for an electrode array. Due to the small dimensions of the fabricated single electrodes, the third aforementioned diffusion regime cannot be reached by variation of scan rate. For an electrode radius of 175 nm, the characteristic frequency specifying the transition is 25 kHz corresponding to a scan rate of 20 kV/s for a scanned potential window of 0.8 V as in Figure 3; a scan rate not achievable with conventional electrochemical setups.

Impedance Spectroscopy. Additional to cyclic voltammetry, electrochemical impedance spectroscopy (EIS) was performed in order to investigate characteristic properties of the fabricated NEE and NEA. To draw an

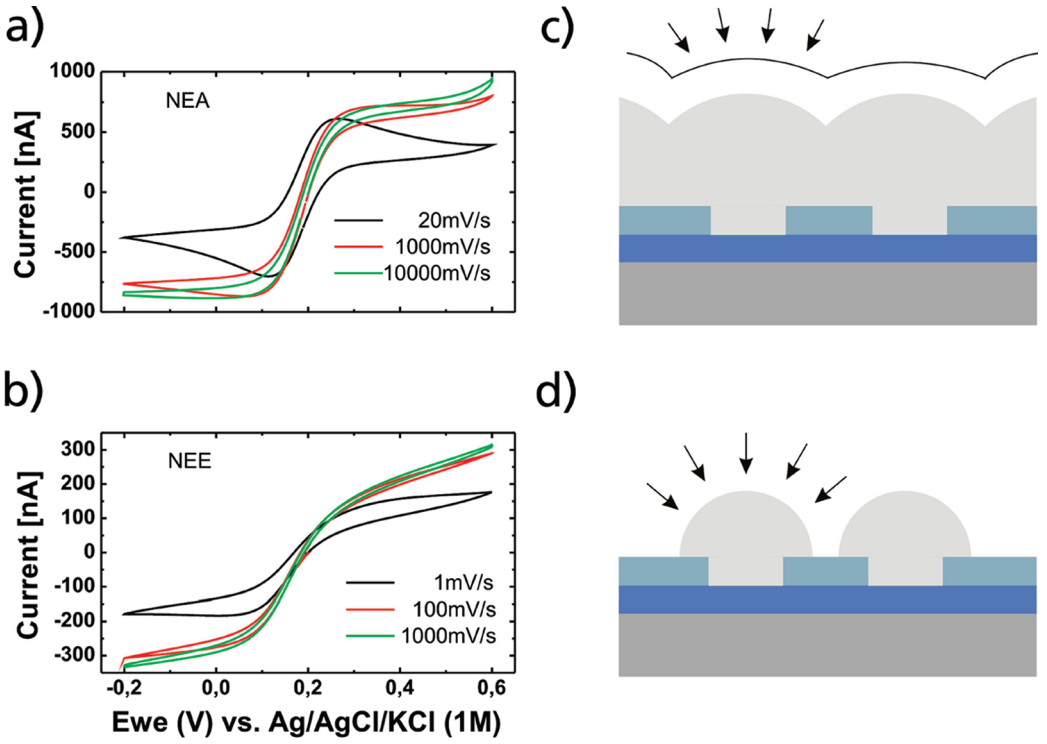

Figure 3. Cyclic voltammograms of 1 mM $Fe(CN)_6^{-3/-4}$ in 0.1 M KCl shown for (a) the NEA with electrode radius 250 nm and distance 10 μm and (b) a NEE with electrode radius 175 nm and a density of electrodes of 8.5×10^5 cm^{-2}. The graphs show the variation of scan rate of the electrochemical experiment determining the diffusion layer thickness. Schematics of the diffusion to small electrodes in the case of overlapping and non-overlapping diffusion hemispheres are shown in (c) and (d), respectively.

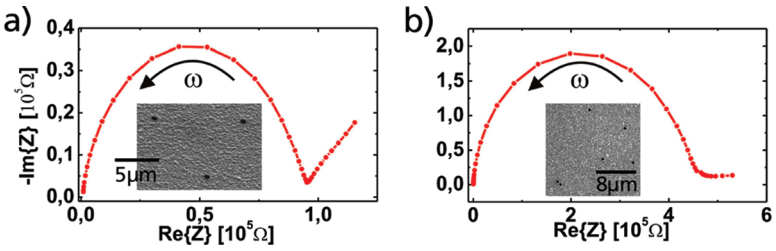

Figure 4. Impedance spectra at open circuit potential of 1 mM $Fe(CN)_6^{-3/-4}$ in 0.1 M KCl for (a) the nanoelectrode array with 250 nm electrode radius and (b) the nanoelectrode ensemble with radii of 175 nm with insets of the distribution and dimensions of the array and the ensemble, respectively.

accurate conclusion from the measured impedance spectra, the characteristic impedance plot of a planar macroscopic electrode will be discussed. For high frequencies, the impedance is governed by the charge transfer resistance related to the electron transfer rate of a specific redox molecule on an electrode surface. A semicircle is the characteristic feature in the impedance spectrum. At low frequencies, on the other hand, mass transfer control or diffusion limitation is observed. For a planar electrode, linear diffusion occurs, and in the diffusion-limited regime for low frequencies, this results in a line with unity slope in the Nyquist plot of the imaginary and real part of the impedance Z.

In this study, the impedance spectra of the NEA and the NEE show similar characteristic features, as shown in the graphs in Figure 4a,b. Both graphs display a large semicircle in the high-frequency regime. At low frequencies, a transition to linear diffusion with unity slope occurs, particularly observable for the NEA in Figure 4a. Theoretical work on the diffusion to microdisk electrodes and the corresponding impedance spectra show that, in the case of three-dimensional hemispherical diffusion, the impedance spectrum will show a semicircle[19,30−32] for frequencies in the interval given by the two mentioned characteristic frequencies $\omega = D/d^2$ and $\omega = D/a^2$. The region for low frequencies of the impedance spectrum therefore represents the regime of overlapping diffusion hemispheres. Obviously the change from typical three-dimensional diffusion to overlapping diffusion hemispheres in Figure 4a is very distinct for the NEA. This is expected

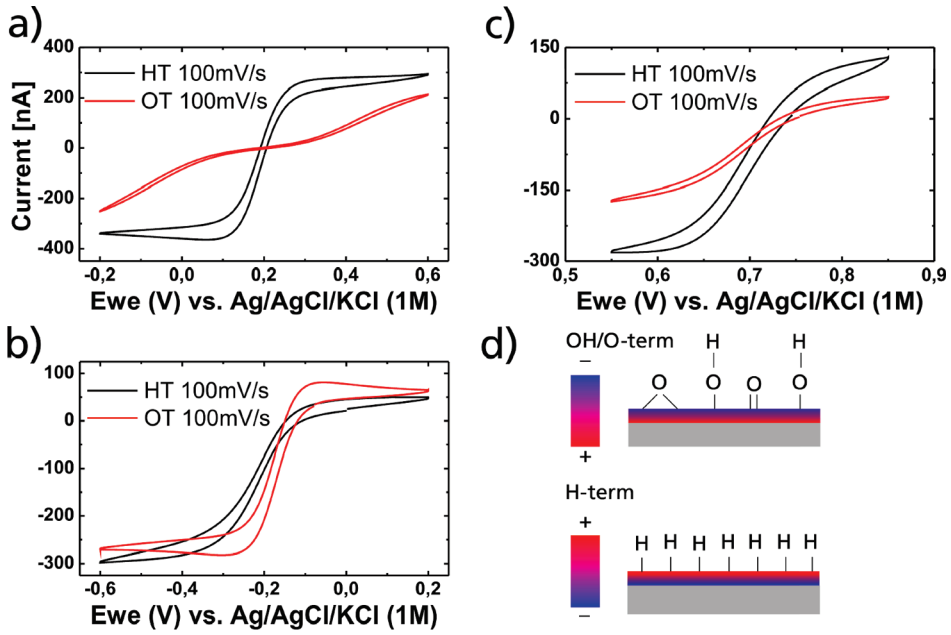

Figure 5. Comparison of voltammograms of (a) $Fe(CN)_6^{-3/-4}$, (b) $Ru(NH_3)_6^{+2/+3}$, and (c) $IrCl_6^{-2/-3}$ on hydrogen- (HT) and oxygen (OT)-terminated all-diamond NEAs. A clear difference between voltammograms on hydrogen- and oxygen-terminated electrode surface is observed depending on the charge of the analyte. A schematic of the charge distribution on a hydrogen- and oxygen-terminated surface is given in (d).

due to well-defined dimensions of the structure from e-beam lithography. For the NEE in Figure 4b, on the other hand, the statistical distribution of electrodes results in a smeared transition. Thus impedance spectroscopy can be utilized to determine average distances between adjacent electrodes.[32]

From the literature, it is known that the impedance semicircle decreases with the number of electrodes and inversely scales with the square of the radius of a single electrode.[19,32] By varying the electrode radius and electrode distance, one can tailor the impedance spectra for a specific biosensing application. The spectra obtained can then be simply described by means of a Randles circuit with a capacitance, charge transfer resistance, solution resistance or a Warburg element, which is for linear diffusion distinct from that for hemispherical diffusion. In a biosensing application, one could, for example, directly monitor the density of linker molecules bound to the electrode surface.

Electrostatic Influence on Electron Transfer Depending on Surface Termination. In the third part of this study, we used a NEA device with electrode radius of 150 nm to measure different redox analytes such as $Ru(NH_3)_6^{+2/+3}$, $Fe(CN)_6^{-3/-4}$, and $IrCl_6^{-2/-3}$ to determine the suitability of the electrochemical sensor for different molecules. In this experiment, we qualitatively compare the electron transfer characteristics corresponding to the shape of the sigmoidal voltammogram with respect to hydrogen- and oxygen-terminated surfaces. The termination of the diamond electrode surface was carried out as described in the Methods section. It is important to point out that by this procedure the nanoelectrode surface can be terminated selectively either with hydrogen or with hydroxyl or carboxyl groups.[34] Figure 5 shows the comparison of voltammograms for each analyte.

For $Fe(CN)_6^{-3/-4}$ displayed in Figure 5a, the electron transfer rate will drastically decrease upon the change from hydrogen- to oxygen-terminated surfaces given by the slope of the transition from reduction to oxidation. This phenomenon is known from studies on macroscopic planar diamond electrodes. Granger *et al.* report that the electron transfer rate constant of $Fe(CN)_6^{-3/-4}$ is strongly dependent on the chemical composition of the diamond electrode surface.[35] Hydrogen-terminated surfaces offer sites for the analyte to perform fast electron transfers. For the NEA, we observe a similar but even more pronounced effect as in Figure 5a. For the hydrogen-terminated surface, we obtain a sigmoidal voltammogram with a fast electron transfer rate. For the anodically treated surface, on the other hand, the steady state is not even observed in the investigated potential window. The currents drop, and the electron transfer for the redox couple is strongly inhibited. The possible effects responsible for the decrease of electron transfer rate constant upon oxygenation of the electrode surface are either an electrostatic or a site blocking effect.

To investigate an electrostatic effect in more detail, responses of $Ru(NH_3)_6^{+2/+3}$ and $IrCl_6^{-2/-3}$ were examined for oxygen- and hydrogen-terminated surfaces, as shown in Figure 5b,c, respectively. In Figure 5d, diamond surfaces are schematically shown with the

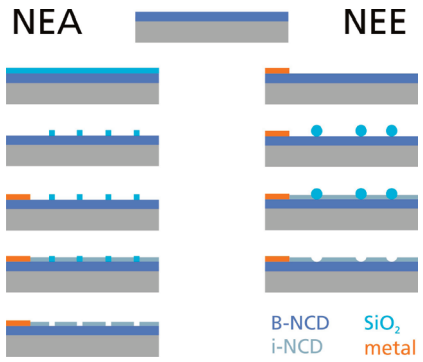

Figure 6. Process steps for the fabrication of all-diamond NEA (left) and NEE (right).

hydrogen-terminated surface with positive surface dipole layer ("positive" refers to the interface of diamond to the liquid) and the oxygen-terminated surface that results in negative surface dipole layer. Both analytes show no difference in the electron transfer rate constant on planar macroscopic diamond electrodes for hydrogen or oxygen termination,[35] which has also been confirmed on a macroscopic planar electrode without any nanostructuring. A macroscopic diamond electrode shows a higher degree of inhomogeneity with respect to boron-doping level and termination effects due to its macroscopic dimensions. For the investigated NEA, one would expect a homogenized behavior due to the small grains of the NCD films as well as a more effective termination of the small electrochemical active area.

Examining $IrCl_6^{-2/-3}$, we expect a similar behavior upon a change of surface termination as seen for $Fe(CN)_6^{-3/-4}$ due to the negative charge: as presented in Figure 5c, the anion $IrCl_6^{-2/-3}$ shows a fast electron transfer on the hydrogen-terminated surface, while at the oxygen-terminated surface, the steady-state current as well as the slope of the transition from reduction to oxidation decreases, indicative of a slower electron transfer.

Finally, for the redox molecule $Ru(NH_3)_6^{+2/+3}$, the opposite effect is observed as expected for an electrostatic influence on the electron transfer rate constant (Figure 5b). The electron transfer rate for $Ru(NH_3)_6^{+2/+3}$ on an oxygen-terminated diamond surface is faster than on a hydrogen-terminated one. This effect for $IrCl_6^{-2/-3}$ and $Ru(NH_3)_6^{+2/+3}$ is small compared to the one for $Fe(CN)_6^{-3/-4}$, indicating that the electron transfer kinetics of the latter are influenced by both a strong site blocking effect and a weak electrostatic effect.[35]

CONCLUSIONS

In this work, the combination of the excellent electrochemical properties of diamond with nanostructuring techniques has been demonstrated to fabricate all nanocrystalline diamond nanoelectrode arrays and ensembles. The resulting arrays and statistical ensembles show sigmoidal voltammograms and impedance spectra explainable by hemispherical diffusion to nanoelectrodes. Furthermore, diamond as an electrode material provides excellent electrochemical properties since it is chemically stable, biofunctionalizable, and offers stable specific surface terminations.

Altering an oxygen-terminated electrode array to a hydrogen-terminated one results in a change of the electron transfer rate constant depending on the sign of the charge of the analyte molecule. This effect could not be observed on macroscopic planar diamond electrodes and emphasizes the sensitivity of the all-diamond NEAs and NEEs. Therefore, the NEAs and NEEs in combination with the efficiency and suitability of the selective electrochemical surface termination offer a new versatile system for electrochemical sensing. In particular, the NEE fabricated by nanosphere lithography offers a cheap and simple alternative to e-beam lithography to obtain electrodes of a few hundreds of nanometers or less.

METHODS

Fabrication of NEAs and NEEs. Two approaches were used to fabricate electrode arrays and ensembles in the range of a few hundred nanometers: 200 nm thin nanocrystalline diamond (NCD) films were grown on 3 in. silicon substrates in an ellipsoid reactor using microwave-assisted chemical vapor deposition. Insulating NCD growth was performed using a conventional H_2/CH_4 plasma with a methane admixture of 1 or 2%. Boron-doping of NCD films was controlled by adding trimethylboron (TMB) to the gas phase with B/C ratios of 6000 ppm. This TMB admixture resulted in metallically doped NCD films with boron concentrations of 1 to 4 $\times$ 10^{21} cm^{-3} as measured by secondary ion mass spectroscopy.[36] Nucleation densities of more than 10^{11} cm^{-2} were achieved by seeding in nanodiamond aqueous colloids. In this process, wafers were immersed in diamond colloids of average size of 5 nm in an ultrasonic bath for 30 min.[37] Topographical, mechanical, electrical, as well as electrochemical properties of grown films have been studied in detail elsewhere and are summarized in several publications.[35,36]

The first approach to fabricate all-diamond NEAs with defined geometrical design used e-beam lithography. The fabrication process steps are schematically shown in Figure 6. On a 200 nm thin boron-doped NCD film, a 200 nm thick PECVD SiO_2 was deposited. This oxide layer was structured using e-beam lithography with subsequent nickel deposition and SF_6 etching of SiO_2. In the next step, metal contacts were deposited using photolithography to allow electrical contact for electrochemical characterization. In the crucial step, a 140 nm thin insulating NCD film was grown on the part of the boron-doped NCD layer that was exposed to the CVD plasma and not protected by SiO_2 islands. With the removal of SiO_2 in hydrofluoric acid, arrays of recessed boron-doped NCD electrodes surrounded by insulating diamond were obtained. The density of electrodes was determined by the design and was 11 $\times$ 10^5 cm^{-2} with a total number of electrodes of 18 000. The

interelectrode distance was 10 μm for all arrays, while the electrode radii were varied from 150 to 250 nm.

The second, cheap, and simple way to fabricate NEEs utilized nanosphere lithography. Initially, a photolithography step was used to deposit metal contacts. Thereafter, samples were immersed in a solution of SiO_2 spheres (G.Kisker GbR) with a radius of 500 nm. In an ultrasonic bath, an equilibrium between spheres sticking to and leaving the sample surface occurs. Thus the concentration of the solution is directly correlated to the density of spheres on the sample surface as well as to the average distance of neighboring spheres. To obtain sigmoidal voltammograms, we chose a concentration 9.55×10^8 cm^{-3}, corresponding to a surface density of 9.7×10^5 cm^{-2} and an average distance of neighboring spheres of $\sim$10 μm. The next step involved the growth of insulating diamond around the above-mentioned spheres shown in Figure 1B. Insulating diamond selectively grew on the area exposed to the plasma. After removal of the SiO_2 spheres in hydrofluoric acid, we obtained electrodes of a concave shape. Electrode radii of 175 nm were achieved with spheres of 500 nm radius, suggesting that further scaling down the electrode size is possible.

Electrochemical Characterization and Termination. Electrochemical experiments were conducted using a Biologic VMP3 potentiostat in a three-electrode setup using a Pt-coil as a counter electrode and a Ag/AgCl/KCl as a reference electrode. The all-diamond NEA and NEE were contacted as the working electrode. Cyclic voltammograms were recorded in 1 mM $Fe(CN)_6^{-3/-4}$ in 0.1 M KCl, 1 mM $Ru(NH_3)^{+3}$ in 0.1 M KCl and 1 mM $IrCl_6^{-2}$ in 0.1 M KCl. Impedance spectroscopy was carried out in 1 mM $Fe(CN)_6^{-3/-4}$/0.1 M KCl at open circuit potential. Impedances were recorded in the frequency interval between 0.1 Hz and 200 kHz at an amplitude of 10 mV. Prior to electrochemical measurements, samples were acid cleaned in H_2SO_4/HNO_3 (3:1, 200 °C, 2 h) and rinsed in DI water. Other than that, no pretreatment for cyclic voltammetry or impedance spectroscopy is necessary.

In experiments, the surface termination of the diamond surface of the working electrode is one of the key parameters since electron transfer kinetics for certain redox molecules strongly depend on the termination.[35] In order to hydrogen terminate the sample surface, a cathodic treatment in an acidic solution (2 M H_2SO_4, -35 V) was carried out while an oxygen-terminated surface was obtained by an anodic treatment at $+3$ V in 2 M H_2SO_4.[34] Reference experiments with hydrogen-terminated surfaces in a hydrogen plasma as well as oxygen-terminated surfaces from acid or oxygen plasma treatment were also performed.

Conductive AFM. AFM measurements are carried out using a Veeco Multimode V. From conductive AFM analysis with a boron-doped diamond-coated silicon tip from Nanosensors, one obtains information about the insulating properties of the NCD surface and the size of the conductive electrode area.

Acknowledgment. This work was supported by the Fraunhofer Attract award "Hybrid HF-MEMS Filters for GHz-Communication and capillary MEMS systems for chemical and biochemical Sensing - COMBIO".

REFERENCES AND NOTES

1. Arrigan, D. W. M. Nanoelectrodes, Nanoelectrode Arrays and Their Applications. *Analyst* **2004,** *129*, 1157–1165.
2. Huang, X. J.; O'Mahony, A. M.; Compton, R. G. Microelectrode Arrays for Electrochemistry: Approaches to Fabrication. *Small* **2009,** *5*, 776–788.
3. Sandison, M. E.; Cooper, J. M. Nanofabrication of Electrode Arrays by Electron-Beam and Nanoimprint Lithographies. *Lab Chip* **2006,** *6*, 1020–1025.
4. Lanyon, Y. H.; Arrigan, D. W. M. Recessed Nanoband Electrodes Fabricated by Focused Ion Beam Milling. *Sens. Actuators, B* **2007,** *121*, 341–347.
5. Lanyon, Y. H.; De Marzi, G.; Watson, Y. E.; Quinn, A. J.; Gleeson, J. P.; Redmond, G.; Arrigan, D. W. M. Fabrication of Nanopore Array Electrodes by Focused Ion Beam Milling. *Anal. Chem.* **2007,** *79*, 3048–3055.
6. Li, H.; Wu, N. A Large-Area Nanoscale Gold Hemisphere Pattern as a Nanoelectrode Array. *Nanotechnology* **2008,** *19*, 275301.
7. Penner, R. M.; Martin, C. R. Preparation and Electrochemical Characterization of Ultramicroelectrode Ensembles. *Anal. Chem.* **1987,** *59*, 2625–2630.
8. Menon, V. P.; Martin, C. R. Fabrication and Evaluation of Nanoelectrode Ensembles. *Anal. Chem.* **1995,** *67*, 1920–1928.
9. Yang, M.; Qu, F.; Lu, Y.; He, Y.; Shen, G.; Yu, R. Platinum Nanowire Nanoelectrode Array for the Fabrication of Biosensors. *Biomaterials* **2006,** *27*, 5944–5950.
10. Lohmüller, T.; Muller, U.; Breisch, S.; Nisch, W.; Rudorf, R.; Schuhmann, W.; Neugebauer, S.; Kaczor, M.; Linke, S.; Lechner, S.; Spatz, J.; Stelzle, M. Nano-porous Electrode Systems by Colloidal Lithography for Sensitive Electrochemical Detection: Fabrication Technology and Properties. *J. Micromech. Microeng.* **2008,** *18*, 115011.
11. Jeoung, E.; Galow, T. H.; Schotter, J.; Bal, M.; Ursache, A.; Tuominen, M. T.; Stafford, C. M.; Russell, T. P.; Rotello, V. M. Fabrication and Characterization of Nanoelectrode Arrays Formed *via* Block Copolymer Self-Assembly. *Langmuir* **2001,** *17*, 6396–6398.
12. Wang, C.; Shao, X.; Liu, Q.; Mao, Y.; Yang, G.; Xue, H.; Hu, X. One Step Fabrication and Characterization of Platinum Nanopore Electrode Ensembles Formed *via* Amphiphilic Block Copolymer Self-Assembly. *Electrochim. Acta* **2006,** *52*, 704–709.
13. Wang, C.; Liu, Q.; Shao, X.; Yang, G.; Xue, H.; Hu, X. One Step Fabrication of Nanoelectrode Ensembles Formed *via* Amphiphilic Block Copolymers Self-Assembly and Selective Voltammetric Detection of Uric Acid in the Presence of High Ascorbic Acid Content. *Talanta* **2007,** *71*, 178–185.
14. Li, J.; Koehne, J.; Cassell, A.; Chen, H.; Ng, H.; Ye, Q.; Fan, W.; Han, J.; Meyyappan, M. *Inlaid Multi-Walled Carbon Nanotube Nanoelectrode Arrays for Electroanalysis*; Wiley-VCH: Verlag, Germany, 2005; Vol. 17, pp 15−27.
15. Koehne, J.; Li, J.; Cassell, A. M.; Chen, H.; Ye, Q.; Ng, H. T.; Han, J.; Meyyappan, M. The Fabrication and Electrochemical Characterization of Carbon Nanotube Nanoelectrode Arrays. *J. Mater. Chem.* **2004,** *14*, 676–684.
16. Tu, Y.; Lin, Y.; Yantasee, W.; Ren, Z. *Carbon Nanotubes Based Nanoelectrode Arrays: Fabrication, Evaluation, and Application in Voltammetric Analysis*; Wiley-VCH: Verlag, Germany, 2005; Vol. 17, pp 79−84.
17. Siddiqui, S.; Arumugam, P. U.; Chen, H.; Li, J.; Meyyappan, M. Characterization of Carbon Nanofiber Electrode Arrays Using Electrochemical Impedance Spectroscopy: Effect of Scaling Down Electrode Size. *ACS Nano* **2010,** *4*, 955–961.
18. Guo, J.; Lindner, E. Cyclic Voltammograms at Coplanar and Shallow Recessed Microdisk Electrode Arrays: Guidelines for Design and Experiment. *Anal. Chem.* **2009,** *81*, 130–138.
19. Fleischmann, M.; Pons, S.; Daschbach, J. The AC Impedance of Spherical, Cylindrical, Disk and Ring Microelectrodes. *J. Electroanal. Chem.* **1991,** *17*, 1–26.
20. Bond, A. M.; Fleischmann, M.; Robinson, J. Electrochemistry in Organic Solvents without Supporting Electrolyte Using Platinum Microelectrodes. *J. Electroanal. Chem.* **1984,** *168*, 299–312.
21. Bond, A. M.; Lay, P. A. Cyclic Voltammetry at Microelectrodes in the Absence of Added Electrolyte Using a Platinum Quasi-Reference Electrode. *J. Electroanal. Chem.* **1986,** *199*, 285–295.
22. Hupert, M.; Muck, A.; Wang, J.; Stotter, J.; Cvackova, Z.; Haymond, S.; Show, Y.; Swain, G. M. Conductive Diamond Thin-Films in Electrochemistry. *Diamond Relat. Mater.* **2003,** *12*, 1940–1949.
23. Nebel, C. E.; Rezek, B.; Shin, D.; Uetsuka, H.; Yang, N. Diamond for Bio-sensor Applications. *J. Phys. D: Appl. Phys.* **2007,** *40*, 6443.
24. Hartl, A.; Schmich, E.; Garrido, J. A.; Hernando, J.; Catharino, S. C. R.; Walter, S.; Feulner, P.; Kromka, A.; Steinmuller, D.; Stutzmann, M. Protein-Modified Nanocrystalline

Diamond Thin Films for Biosensor Applications. *Nat. Mater.* **2004,** *3*, 736–742.
25. Yang, W.; Auciello, O.; Butler, J. E.; Cai, W.; Carlisle, J. A.; Gerbi, J. E.; Gruen, D. M.; Knickerbocker, T.; Lasseter, T. L.; Russell, J. N.; Smith, L. M.; Hamers, R. J. DNA-Modified Nanocrystalline Diamond Thin-Films as Stable, Biologically Active Substrates. *Nat. Mater.* **2002,** *1*, 253–257.
26. Provent, C.; Haenni, W.; Santoli, E.; Rychen, P. Boron-Doped Diamond Electrodes and Microelectrode-Arrays for the Measurement of Sulfate and Peroxodisulfate. *Electrochim. Acta* **2004,** *49*, 3737–3744.
27. Pagels, M.; Hall, C. E.; Lawrence, N. S.; Meredith, A.; Jones, T. G. J.; Godfried, H. P.; Pickles, C. S. J.; Wilman, J.; Banks, C. E.; Compton, R. G.; Jiang, L. All-Diamond Microelectrode Array Device. *Anal. Chem.* **2005,** *77*, 3705–3708.
28. Soh, K. L.; Kang, W. P.; Davidson, J. L.; Basu, S.; Wong, Y. M.; Cliffel, D. E.; Bonds, A. B.; Swain, G. M. Diamond-Derived Microelectrodes Array for Electrochemical Analysis. *Diamond Relat. Mater.* **2004,** *13*, 2009–2015.
29. Colley, A. L.; Williams, C. G.; D'Haenens Johansson, U.; Newton, M. E.; Unwin, P. R.; Wilson, N. R.; Macpherson, J. V. Examination of the Spatially Heterogeneous Electroactivity of Boron-Doped Diamond Microarray Electrodes. *Anal. Chem.* **2006,** *78*, 2539–2548.
30. Fleischmann, M.; Pons, S. The Behavior of Microdisk and Microring Electrodes. Mass Transport to the Disk in the Unsteady State: The AC Response. *J. Electroanal. Chem.* **1988,** *250*, 277–283.
31. Abrantes, L. M.; Fleischmann, M.; Peter, L. M.; Pons, S.; Scharifker, B. R. On the Diffusional Impedance of Microdisc Electrodes. *J. Electroanal. Chem.* **1988,** *256*, 229–233.
32. Köster, O.; Schuhmann, W.; Vogt, H.; Mokwa, W. Quality Control of Ultra-microelectrode Arrays Using Cyclic Voltammetry, Electrochemical Impedance Spectroscopy and Scanning Electrochemical Microscopy. *Sens. Actuators, B* **2001,** *76*, 573–581.
33. Hepel, T.; Osteryoung, J. Electrochemical Characterization of Electrodes with Submicrometer Dimensions. *J. Electrochem. Soc.* **1986,** *133*, 757.
34. Hoffmann, R.; Kriele, A.; Obloh, H.; Hees, J.; Wolfer, M.; Smirnov, W.; Yang, N.; Nebel, C. E. Electrochemical Hydrogen Termination of Boron-Doped Diamond. *Appl. Phys. Lett.* **2010,** *97*, 052103-3.
35. Granger, M. C.; Swain, G. M. The Influence of Surface Interactions on the Reversibility of Ferri/Ferrocyanide at Boron-Doped Diamond Thin-Film Electrodes. *J. Electrochem. Soc.* **1999,** *146*, 4551–4558.
36. Gajewski, W.; Achatz, P.; Williams, O. A.; Haenen, K.; Bustarret, E.; Stutzmann, M.; Garrido, J. A. Electronic and Optical Properties of Boron-Doped Nanocrystalline Diamond Films. *Phys. Rev. B* **2009,** *79*, 045206.
37. Williams, O. A.; Douhéret, O.; Daenen, M.; Haenen, K.; Osawa, E.; Takahashi, M. Enhanced Diamond Nucleation on Monodispersed Nanocrystalline Diamond. *Chem. Phys. Lett.* **2007,** *445*, 255–258.